Applied Surface Science 487 (2019) 218–227

Contents lists available at ScienceDirect

Applied Surface Science

journal homepage: www.elsevier.com/locate/apsusc

Full length article

Release of helium-related clusters through a nickel–graphene interface: An atomistic study

Hai Huang[a,b], Xiaobin Tang[a,c,*], Fei Gao[b,**], Feida Chen[a,c], Guojia Ge[a], Yuanyuan Yan[a], Qing Peng[b]

[a] Department of Nuclear Science & Engineering, Nanjing University of Aeronautics and Astronautics, Nanjing 210016, China
[b] Department of Nuclear Engineering and Radiological Science, University of Michigan, Ann Arbor, MI 48109, USA
[c] Jiangsu Engineering Laboratory of Nuclear Energy Equipment Materials, Nanjing 210016, China

ARTICLE INFO

Keywords:
Nickel–graphene interface
Helium embrittlement
Clusters
Segregation
Atomistic simulation

ABSTRACT

Nickel–graphene nanolayers with high-density interfaces are expected to have excellent resistance to helium (He) embrittlement and proposed as candidate materials for molten salt reactor systems. However, He irradiation effects on nickel–graphene nanolayers remains poorly understood at present. In this work, the influence of a nickel–graphene interface (NGI) on the nucleation and growth of He-related clusters was studied by using atomistic simulations. The NGI reduces formation energies and diffusion energy barriers for He-related clusters. The reduction makes He-related clusters easily be trapped by the interface, thus leading to significant segregation. Consequently, He concentration in the bulk is considerably reduced, and the nucleation and growth rates of He-related clusters in the bulk are delayed. Owing to the high mobility of He-related clusters at the NGI, these clusters easily coalesce to form larger clusters than those in the bulk. A reasonable design of nanolayers may promote He releasing from materials. Results of the current study can provide fundamental support for the service life assessment of nickel–graphene nanolayers in extreme environments.

1. Introduction

Metal–graphene (Gr) nanolayers have been developed in the past few years and gradually proven to have excellent radiation tolerance [1–5], since the nanolayers are rich in metal–Gr interfaces that can provide abundant sinks for trapping radiation-induced defects and centers for defect recombination [6–12]. Si et al. [1] found that small-period-thickness tungsten–Gr nanolayers exhibit high radiation tolerance in the reduction of helium (He) bubble density. Kim et al. [2] observed that vanadium–Gr nanolayers can effectively reduce radiation-induced hardening and suppress brittle failure compared with its pure counterpart after He irradiation with a dose of 13.5 displacements per atom (dpa). Huang et al. [3] demonstrated that nickel–Gr interfaces (NGIs) play an important role in reducing lattice swelling and stacking faults induced by He irradiation. So et al. [4] indicated that aluminum–Gr interfaces considerably reduce radiation hardening and embrittlement under He irradiation at a dose of up to 72 dpa. Therefore, the nanolayers are expected to have enormous potential applications in the field of He-related (defined as He_n and He_nV_m clusters) engineering.

For a long time, He embrittlement of Ni-based alloys has always plagued the safe operation and long-term service of molten salt reactor (MSR) systems [13–18]. The irradiation degradation is mainly due to the large neutron absorption cross section of Ni [14,18]. Under the reactor neutron irradiation environment, a considerable amount of He atoms produced by a two-step nuclear transmutation reaction ($^{58}Ni + n \rightarrow {}^{59}Ni$, $^{59}Ni + n \rightarrow {}^{56}Fe + {}^{4}He$) is introduced into the materials [14,16]. Given the extremely low solubility in metallic materials [14,16,19], He atoms tend to be trapped at small vacancy (V) clusters and other microstructural features, resulting in the creation of He-stabilized bubbles and the further coarsening of these bubbles at elevated temperatures [19–23]. Current Ni-based alloys rarely withstand the extreme irradiation [13,14,24]. New design concepts for materials that can resist damage under extreme irradiation are still needed, which will further improve the lifetime of materials and enhance the safety of nuclear reactors. Consequently, metal–Gr nanolayers provide an excellent solution for the above stringent requirements. Especially, Ni–Gr nanolayers (NGNLs) with high-density NGIs become candidate materials for the MSR to improve the He irradiation embrittlement resistance. However, in comparison to Ni-based alloys, there is much less experience with the effects of He irradiation on NGNLs, and the

* Correspondence to: X. Tang, Department of Nuclear Science & Engineering, Nanjing University of Aeronautics and Astronautics, Nanjing 210016, China.
** Corresponding author.
E-mail addresses: tangxiaobin@nuaa.edu.cn (X. Tang), gaofeium@umich.edu (F. Gao).

https://doi.org/10.1016/j.apsusc.2019.05.085
Received 13 February 2019; Received in revised form 17 April 2019; Accepted 7 May 2019
Available online 09 May 2019
0169-4332/

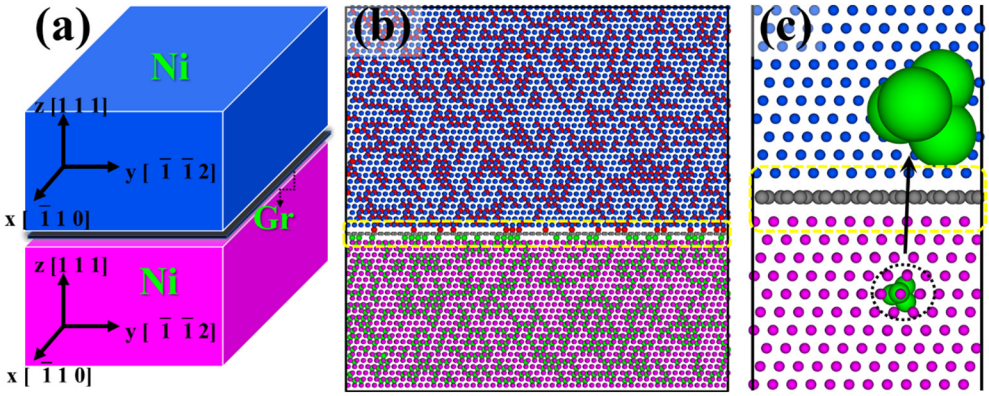

Fig. 1. Simulation model. (a) Conceptual schematic simulation cell of NGNLs. (b) Atomic configuration of NGNLs with 934 He atoms. (c) Atomic configuration of NGNLs with a He_4V cluster. The spheres are presented in different colors and sizes to facilitate visualization. The pink (or blue), gray, and green (or red) spheres represent Ni, C, and He atoms in the cell, respectively. The NGI region, which contains one Gr plane and two terminal Ni planes near the Gr, is indicated by a yellow dashed box.

fundamental knowledge is still lack at present.

Predicting the He damage behaviors of materials requires understanding the interactions of He with different defect structures [23,25–31], that is, the clustering mechanisms of He atoms around vacancies, including the formation of He_nV_m clusters and subsequent bubble growth [25,27,28], as well as the interactions of He-related clusters with other defects, such as grain boundaries (GBs) and heterointerfaces [23,26,29,31]. Computer simulations provide important insights into the fundamental understanding of complex atomic-level processes of He clustering and the interaction of these clusters with other defects. For example, by using molecular dynamics (MD) simulations, Yang et al. [23] investigated the accumulation and clustering of He atoms at GBs in α-Fe. They found that the formation of He clusters accompanies with the emission of self-interstitial atoms (SIAs) collected at the periphery of these clusters, and the product of the density and average size of He clusters is approximately the same in bulk and GB regions. Torres et al. [32] indicated that He atoms are mainly accumulated in the vicinity of Ni GB plane at the temperature of 600 K. By using molecular statics (MS) calculations, Li et al. [25] and Torres et al. [33] respectively demonstrated that the binding energy between He atom and He cluster is positive and increases with increasing He cluster size in W and Ni. Li et al. [25] also found that the He cluster formation in W can be promoted by the SIAs and vacancies. Hu et al. [34] presented an analysis of the interactions of He_n clusters with W GBs and revealed that the cluster–GB interactions are responsible for the cluster migration by drift and He segregation on GBs. The calculations of Tschopp et al. [35] showed that the binding energy of an additional He atom in a He_nV cluster is considerably affected by the α-Fe GB environment relative to the same cluster in bulk, and the binding energy for an additional He atom is larger away from the GB center as the size of He_nV cluster increases. Gong et al. [36] revealed that the binding energy of an interstitial He atom to He_nV_m is generally larger in pure Ni than that in the Ni GB, the Ni vacancy possesses a higher trapping strength to He_n compared with that in Ni GB, and the binding strength of He_n to Ni GB is stronger than that of He_nV_m to the GB. McPhie et al. [31] found that He_nV clusters are stable against dissociation and recombination and thus reduce combination possibilities with other defects to release the He atoms, due to the interstitial-emission process and the high binding energies of SIAs to Cu—Nb interfaces. Therefore, understanding the effects of NGIs on the nucleation and growth of He-related clusters by atomistic simulations is of fundamental importance to develop NGNLs resisting helium embrittlement for the MSR.

In this work, we investigated the effects of NGIs on the nucleation and growth of He-related clusters from the thermodynamic, energetic, and kinetic perspectives. First, a series of dynamic behaviors at the temperature of 800 K, including He clustering, He atom/cluster diffusion, and He atoms/cluster interacting with NGIs, were explored by using MD simulations. Second, the formation energies of He_n/He_nV clusters, the binding energies of He_n/He_nV clusters to NGIs, and the binding energies of an additional He atom to He_{n-1}/$He_{n-1}V$ clusters were calculated with the MS method. The two types of He-related clusters were preferentially considered herein because their configurations are relatively simple such that basic knowledge of the formation/binding properties of He-related clusters can be easily obtained [25,28,33,35]. The formation and binding energies of low-order clusters may actually be an adequate predictor for those of high-order clusters [28]. Furthermore, the migration behaviors of He atoms jumping toward/along NGIs were calculated by using climbing-image nudged elastic band (CI-NEB). Given that the formation of He-related clusters and their interactions in NGNLs are a complex issue, the present study provides important results for future more comparative studies at high scales and enhances our understanding of the thermodynamics, energetics, and kinetics involved in NGIs interaction with He-related clusters and the effects on He embrittlement in NGNLs. The careful design of NGIs is also demonstrated to provide a channel for He releasing from NGNLs.

2. Simulation methodology

2.1. Interatomic interactions and theoretical models

All the calculations were performed with MD code LAMMPS [37], and visualizations were rendered with OVITO [38]. The embedded atom method (EAM) potential developed by Bonny et al. [39] was used to describe the interactions between Ni atoms. The reason for adopting the potential is because it can accurately reproduce point defects in Ni [32]. The interactions among carbon atoms in Gr were described by the adaptive intermolecular reactive empirical bond order (AIREBO) potential [40]. The He—He interactions were modeled by using the Beck potential [41], which reproduces the second virial coefficient for He and is therefore adequate in the present study of He clustering [33]. The Ni—C and He—C interactions were described by 12–6 Lennard–Jones type of van der Waal's potential [7,42–44]. The Ni—He interactions were described by using the Morse-3G interatomic potential [45], which can accurately reproduce the diffusion energy barrier of He, the formation energy of He, and He clustering in Ni [32]. The NGI models used in this work were obtained as follows. Initially, a sandwich model (Fig. 1(a)) was created by using a *top-fcc* configuration. The creation details have been described elsewhere [7]. Subsequently, a conjugate gradient minimization method under zero external pressure was performed to release the stress of the NGI structure. Periodic boundary conditions along the three Cartesian directions were applied in all the calculations.

2.2. MD simulations

The dynamic behaviors of He-related clusters near the NGI during their nucleation and growth were investigated by using a large system comprising 186,992 atoms with a size of 12.52 × 12.96 × 12.56 nm^3. Initially, a He concentration of 4970 appm was produced by randomly inserting 934 He atoms into the Ni tetrahedral interstitial sites (TIS;

Fig. 1[b]), which are the most stable configurations for He atoms in Ni [33,45]. After the insertion, the model was relaxed at 0 K for 10 ps. Subsequently, the temperature was rescaled to a desired value (800 K) and kept as a constant thereafter. The Nose-Hoover thermostat-barostat (NPT) ensemble was employed to obtain a constant temperature by equilibrating the system for 1.01 ns with a timestep of 1 fs and ensure no significant fluctuation of the system pressure. He-related clusters were defined as He atoms within a distance of 0.3 nm, and the Frenkel pairs were detected by using Wigner–Seitz cell method [17].

2.3. MS calculations

A small system with dimensions of 2.49 × 2.59 × 10.12 nm^3 (6000 atoms) was adopted for the investigation of the energetic and kinetic mechanisms of nucleation and growth of He-related clusters near the NGI. The details of the introduction of He_n and He_nV clusters are provided in the Supplementary Material. The present study explored 10 types of He_n/He_nV (n = 1–10) clusters, which are denoted as He_1, He_2, He_3, …, and He_{10} (or He_1V, He_2V, He_3V, …, and $He_{10}V$), where the system with a He_4V cluster is shown in Fig. 1(c). The formation energy of each He_n/He_nV cluster can be given by

$$E_f^{He_nV_m^\alpha} = (E_{NGI}^{He_nV_m^\alpha} + m{\cdot}E_{coh}^{Ni}) - (E_{NGI} + n{\cdot}E_{coh}^{He}), \quad (1)$$

where $E_{NGI}^{He_nV_m^\alpha}$ (E_{NGI}) is the total energy of the simulation cell with (without) the He_n/He_nV cluster at a particular site α, E_{coh}^{Ni} is the cohesive energy per atom in a perfect *fcc* Ni lattice (−4.45 eV), and E_{coh}^{He} is the cohesive energy per atom of an *fcc* He crystal (−0.00703 eV). m = 0/1 denotes the He_n/He_nV cluster, respectively. To quantify the interaction of NGI with the He_n/He_nV cluster, the binding energy can be calculated by comparing the formation energy of He_n/He_nV cluster in the bulk with that within the NGI, and is defined as

$$E_b^{He_nV_m^\alpha} = E_f^{He_nV_m^{\alpha,bulk}} - E_f^{He_nV_m^{\alpha,NGI}}, \quad (2)$$

where $E_f^{He_nV_m^{\alpha,\ bulk}}$ and $E_f^{He_nV_m^{\alpha,\ NGI}}$ are the formation energies of He_n/He_nV clusters in the bulk and within the NGI, respectively. To quantify the interaction of the He_{n-1}/$He_{n-1}V$ cluster with an additional interstitial He atom, the binding energy is calculated by

$$E_b^{He\rightarrow He_{n-1}V_m^\alpha} = (E_f^{He_{n-1}V_m^\alpha} + E_f^{He_1}) - E_f^{He_nV_m^\alpha}, \quad (3)$$

where $E_f^{He_{n-1}V_m^\alpha}$, $E_f^{He_nV_m^\alpha}$, and $E_f^{He_1}$ can be obtained from Eq. (1). In Eq. (3), when n = 1 and m = 0, the binding energy is regarded as zero because this describes a single He atom without other defects. When n = 1 and m = 1, the binding energy represents the interaction strength between an interstitial He atom and a vacancy ($E_f^{V^\alpha}$ = 1.387 eV in the bulk or 0.93 eV within the NGI [7]). Thus, a positive binding energy indicates the attraction of an additional He atom on the He_{n-1}/$He_{n-1}V$ cluster, whereas a negative value means the repulsion between an additional He atom and the He_{n-1}/$He_{n-1}V$ cluster. High binding energy represents strong attractions between them. The similar principle also applies to clarify the interaction strength between the NGI and He_n/He_nV cluster. Note that the minimum formation energy and maximum binding energy of each He_n/He_nV cluster obtained from 20 different instantiations as shown in the Supplementary Material will be discussed hereinafter. In addition, the kinetic details of the optimum migration paths and diffusion energy barriers of He atoms calculated by the CI-NEB method can be compared with those of Frenkel defects described elsewhere [7].

3. Results and discussion

3.1. Dynamic evolution of He-related clusters

The dynamic behaviors of nucleation and growth of He-related clusters in NGNLs at 800 K are shown in Fig. 2. At the initial stage, 934 He atoms are randomly distributed in the simulation box as isolated interstitials at the TIS. At 0.005 ns, a quantity of He atoms crossed the cell boundary and entered their opposite Ni bulk, suggesting that the significant migration of He atoms occurs in the bulk. Meanwhile, small He_n clusters (n varying from 2 to 7) are observed to form, implying that isolated He atoms prefer to attract each other. At 0.01 ns, SIAs and vacancies emerge in the bulk. For example, a He_6 cluster is created at 0.005 ns, together with the emission of a SIA, thus forming a He_6V_1 cluster. A He_7 generated at 0.005 ns captures three nearby He atoms to form a He_{10} without displacing Ni atoms at 0.01 ns. However, the number of isolated He atoms in the vicinity of NGI evidently decreases at 0.03 ns and they tend to be adsorbed by the NGI. Even two He_5 generated at 0.01 ns are also trapped by the NGI at this moment (see Fig. S2). The He_4 generated at 0.01 ns is quickly dissociated, but these He atoms are trapped into the NGI and absorbed by a He_9 cluster, respectively (see Supplementary Movie 1), implying a dynamics competition of He trapping between the NGI and He clusters. Larger He_nV_m clusters (*e.g.*, $He_{12}V_3$) are generally formed by absorbing more He atoms and emitting more Ni atoms, thus creating more vacancies within the He clusters [17,23,46]. This process results in an increased probability for the He clusters to attract isolated He atoms or small He clusters. At 0.05 ns, two Frenkel pairs are produced near the NGI and collected around He clusters. The two SIAs are instantly trapped into the NGI at 0.055 ns, suggesting the role of NGI not only in trapping He but also in trapping Frenkel defects. At 0.11 ns, more SIAs (in the form of clusters) are kicked out and attached to the He clusters, thus leading to the growth of He clusters as described in several previous studies [23,32]. A Frenkel pair close to the upper surface of the NGI is generated at 0.118 ns. This phenomenon may be due to the gathering of a large number of He atoms within the NGI and generation of strong stress on the Ni atoms near the NGI. When the stress exceeds a critical value, the SIA is emitted from the NGI. However, the Frenkel defect pair disappears at 0.12 ns due to the role of the NGI, which also provides a center for defect recombination and annihilation. After 0.12 ns, SIAs and vacancies have been observed to be frequently created and annihilated within the NGI, which is attributed to the dynamic behavior of Frenkel pairs within the NGI. Meanwhile, the centroid positions of He-related clusters in the bulk do not change with time. All isolated He atoms are trapped by the NGI or absorbed by He-related clusters at 0.476 ns. The size and distribution of He-related clusters remain stable until 1.01 ns but with some fluctuations. Only several small He_nV_m clusters (*e.g.*, He_6V_2) are survived near the NGI, and the largest cluster in the bulk contains 27 He atoms and 5 vacancies, that is, a $He_{27}V_5$ cluster. Throughout the MD time scale, isolated He atoms and small He_n clusters continuously coalesce to form large clusters or diffuse toward the NGI. However, once vacancies are created in the He clusters, the He_nV_m configurations become immobile, making it difficult to be trapped by the NGI. The detailed evolution is exhibited in Supplementary Movie 2.

A considerable amount of He atoms flood into the NGI and may induce some peculiarly structural changes within the NGI. The dynamic evolution of He atoms within the NGI is shown in Fig. 3. Initially, isolated He atoms sporadically disperse around the NGI. At 0.01 ns, most of the He atoms close to the NGI are trapped on the surface of the Gr, and the isolated He atoms are easy to migrate and aggregate into clusters, resulting in the formation of several small He_n clusters, such as He_4 and He_5 clusters. At 0.05 ns, those small He clusters act as nucleation sites and trap the isolated He atoms at certain distances away from the clusters. However, not all clusters tend to grow. Conversely, the dissociation of the clusters occurs; for example, the He_5 generated at 0.05 ns dissociates into a He and a He_4 at 0.055 ns. After 0.055 ns, the He clusters can coalesce into larger clusters frequently due to the high mobility of He clusters within the NGI, a behavior that is different from that in the bulk. For example, the He_{16} and a He atom migrate to the site of He_{21}, thus forming a He_{38} at times from 0.095 to 0.1 ns, and the He_{34} and He_{44} coalesce to form a He_{78} at times from 0.128 to 0.13 ns.

Initially, the He_{78} cluster has an ellipse shape at 0.13 ns but quickly rotates to a disk shape that is a stable configuration of a He cluster within the NGI. The He_{31} and an additional He atom are also observed to be trapped by the He_{85} to generate a He_{117} at times from 0.132 to 0.15 ns, resulting in the creation of more SIAs and vacancies around the NGI. During this time, the He_9 and He_{16} incessantly jump toward the He_{117}, thus forming a He_{149} cluster at 0.372 ns. At this moment, all the isolated He atoms disappear, and only two large and four small He clusters are left within the NGI. The large clusters (*e.g.*, He_{149}) are pinned by the vacancies around them. These cluster configurations are maintained until 1.01 ns. The passage of He through the Gr is not observed, demonstrating the impermeability of Gr to He [1,2]. However, with the recombination/annihilation of vacancies with the SIAs near the NGI at a longer time [11], the large clusters will be unpinned and maintained rapid movement along the NGI, eventually absorbing residual small clusters. Compared with the bulk, a low number density of clusters is displayed within the NGI, but the average cluster size is large. Overall, the NGI acts as a sink to continuously trap the He atoms/clusters transported from the bulk and decrease the density and size of He clusters in the bulk; meanwhile, the He atoms entering the NGI can easily migrate to aggregate into large clusters. The detailed evolution of He clustering within the NGI is exhibited in Supplementary Movie 3.

3.2. Formation and binding energies of He_n

As shown in Figs. 2 and 3, He atoms tend to mutually attract and aggregate into clusters either in the bulk or within the NGI, whilst the NGI acts as a sink to trap He atoms/clusters. Revealing the nature of these phenomena requires an energetic perspective, that is, determining the influences of the local environment on the formation and binding of He clusters. The formation and binding energies of He_n clusters as a function of the distance from the NGI are shown in Fig. 4. Among these energies, the formation energy of an isolated He atom at the TIS and octahedral interstitial sites (OIS) in the bulk is 4.50 and 4.67 eV, respectively, in agreement with the values of Torres et al. [45]. This finding confirms that He atom is indeed more stable at the TIS than at the OIS in NGNLs. Similar to the results of SIAs and vacancies [7], the formation and binding energies of He_n clusters remarkably deviate from their values in the bulk as He_n clusters approach the NGI, and are symmetric in relation to the Gr. The formation of He_n is always endothermic as the defects move from the bulk to the NGI. Consequently, the binding energy of He_n in the vicinity of NGI is positive and presents an increasing trend with the increase in n, suggesting that the He_n clusters tend to segregate into the NGI, which is enhanced with the increasing n. In addition, as the number of the He atoms in a He_n cluster

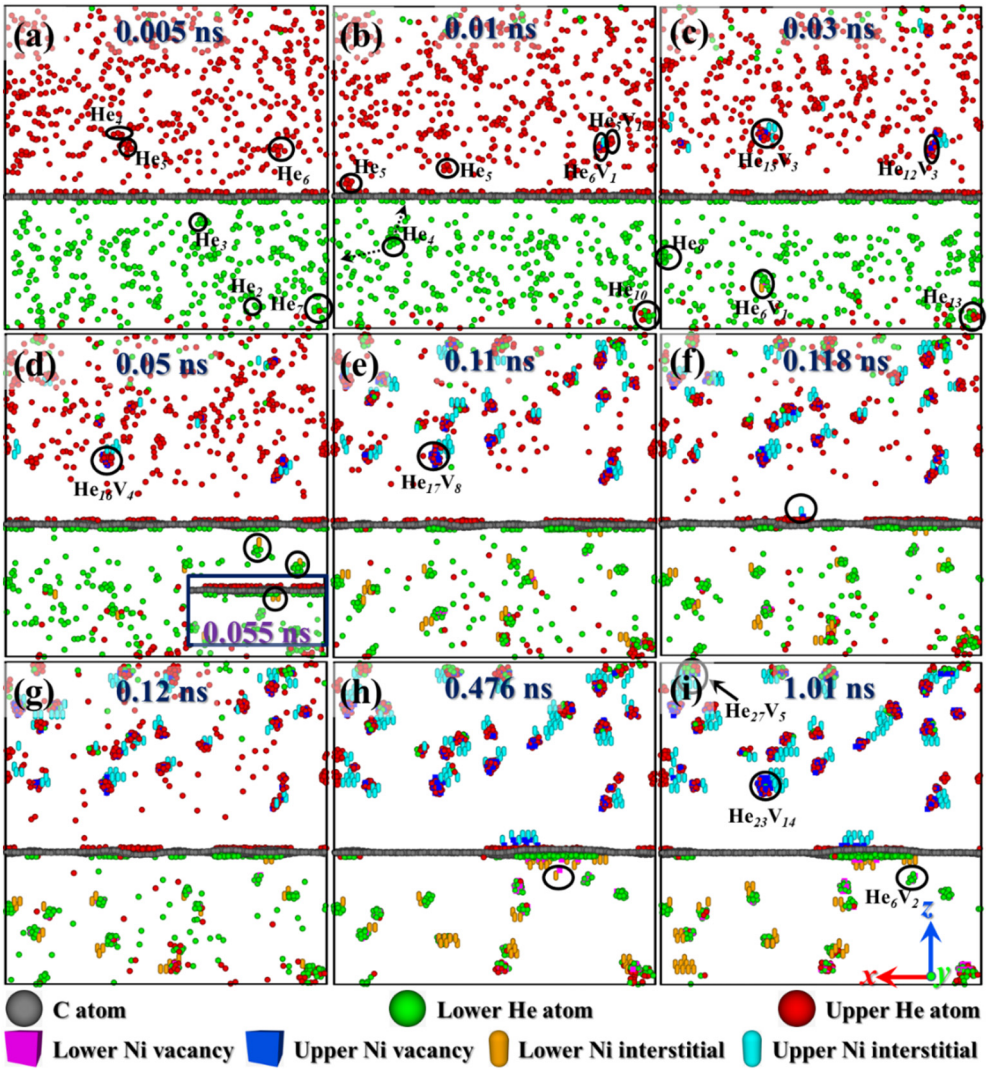

Fig. 2. Snapshots of the dynamic evolution of He clustering near the NGI at the times of 0.005 ns (a), 0.01 ns (b), 0.03 ns (c), 0.05 ns (d), 0.11 ns (e), 0.118 ns (f), 0.12 ns (g), 0.476 ns (h), and 1.01 ns (i). The local region of the model at 0.055 ns is also exhibited in the inset of panel (d). For easy differentiation, the Ni atoms in perfect lattice sites are not shown. The He atoms, vacancies, and SIAs above and below the Gr, as well as C atoms, are displayed in different colors as labeled in the figure. Some typical defects are identified by black circles.

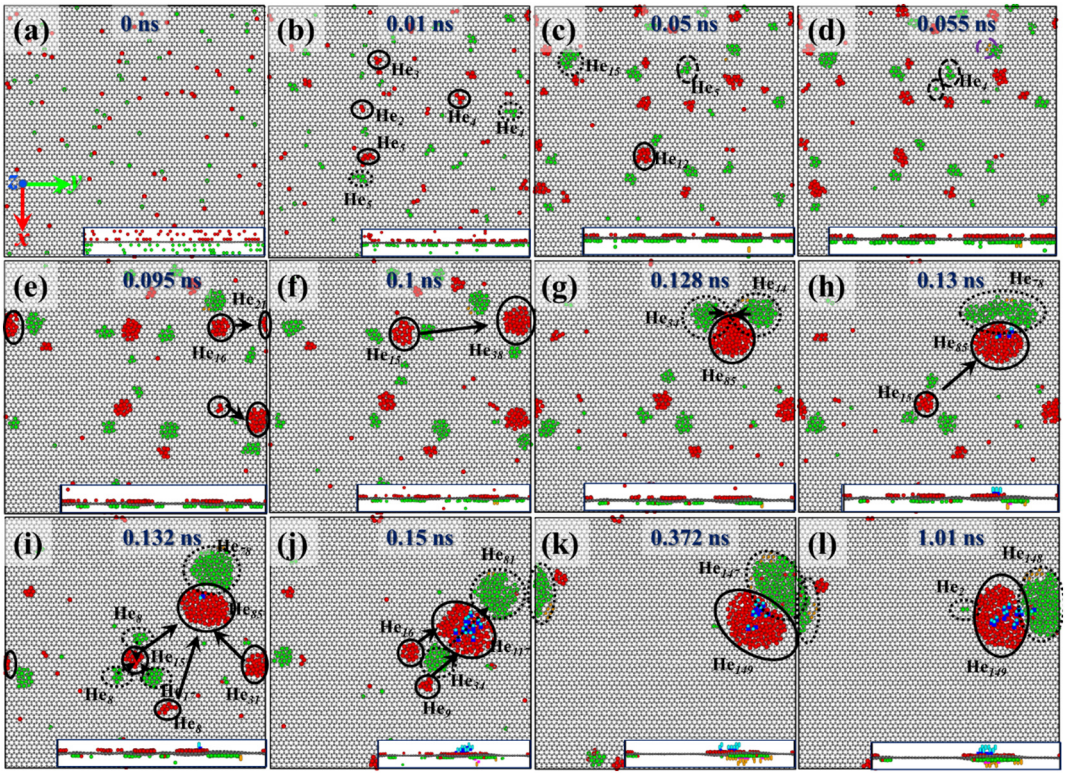

Fig. 3. Snapshots showing the dynamic evolution of He clustering within the NGI at times of 0 ns (a), 0.01 ns (b), 0.05 ns (c), 0.055 ns (d), 0.095 ns (e), 0.1 ns (f), 0.128 ns (g), 0.13 ns (h), 0.132 ns (i), 0.15 ns (j), 0.372 ns (k), and 1.01 ns (l). The side view of each panel is also separately exhibited in the corresponding inset. The identification of different atoms and defects is similar to the legend in Fig. 2. Some typical defects above and below the Gr are identified by black dashed and solid circles, respectively, and their movement tendencies are marked by black arrows.

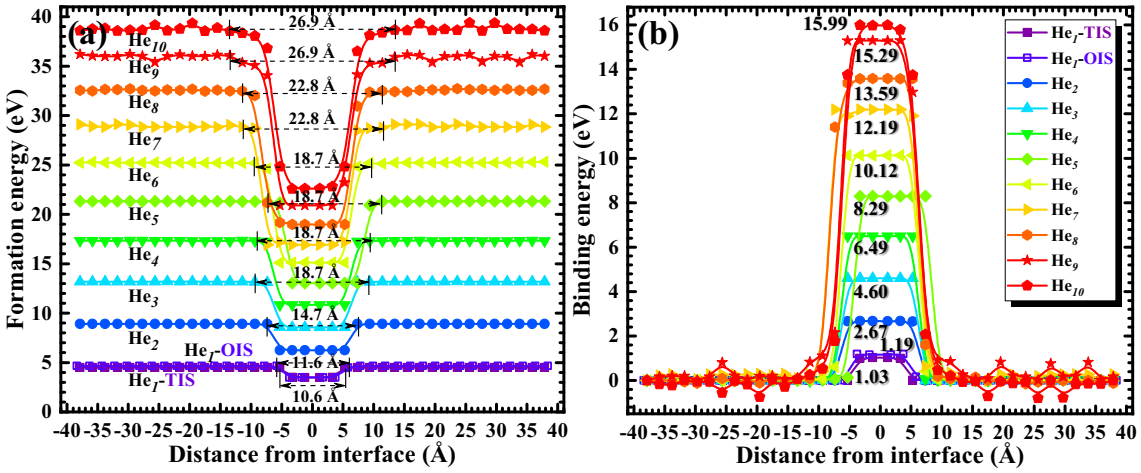

Fig. 4. Formation (a) and binding (b) energies of He_n clusters (n = 1–10) as a function of the distance from the NGI. The interaction length range and binding energy of He_n clusters with the NGI are marked.

increases, the interaction length range of the cluster with the NGI also gradually increases from 10.6 Å (or 11.6 Å) to 26.9 Å (exceeding the width of the NGI (5.5 Å)), indicating that the segregation profile strongly depends on the local environment of He_n. As an example, a He_5 cluster at a distance of 8.9 Å away from the Gr is observed to first induce local expansion, quickly drifted by the NGI, and finally segregated into the NGI after athermal relaxation (see Fig. S4). During this process, the He_5 is transformed from a three-dimensional configuration into a two-dimensional configuration. The drift-segregation model shows relative consistency with the obtained MD results (Fig. 2(b) and (c)) and the finding of Hu et al. [34] in W GB but may possibly be more pronounced as the n increases due to the wide interaction range and high binding energy. The formation and binding energies of He_n clusters in the bulk have a slight fluctuation as the n exceeds 8, along with the analysis of He_n configurations expounded in the Supplementary Material. In this case, the number of He atoms that can be accommodated at an interstitial site has almost saturated. The He_n clusters will excessively displace the surrounding Ni atoms and may even emit SIAs to release stress, resulting in the instability in energetics.

Further energetic information, including the formation energies of He_n in the bulk and within the NGI, the binding energies of an additional He to He_{n-1} in the bulk and within the NGI, and the binding energy of He_n to the NGI for different n, is extracted from Fig. 4 and exhibited in Fig. 5. The formation energy of He_n linearly increases with

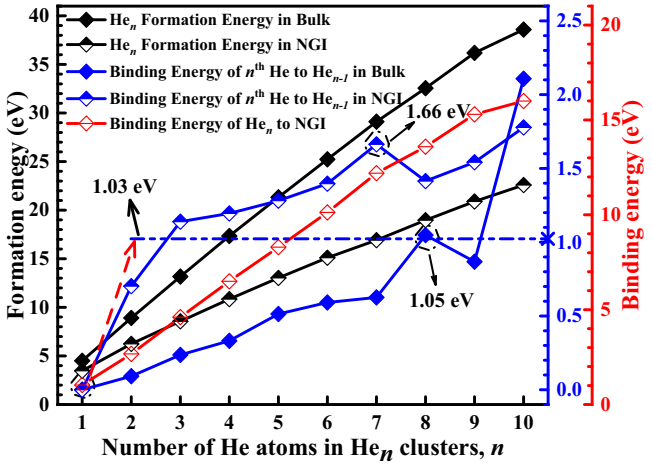

Fig. 5. Energetics of He$_n$ clusters as a function of the number of He atoms, including the formation energies of He$_n$ and the binding energies of an additional He to He$_{n-1}$ in the bulk and within the NGI, as well as the binding energy of He$_n$ to the NGI. The binding energy of a single He atom to the NGI is also highlighted by the blue dashed line.

the increasing number of He atoms whether in the bulk or within the NGI, which is consistent with the results of a previous study [47]. The increase in the interaction range is from 4.50 to 38.58 eV in the bulk or from 3.47 to 22.59 eV within the NGI (see Table S1), and the increasing slope of the dependency is determined to be 3.84 or 2.10 eV/atom, respectively. The low formation energy indicates weak local deformation around the defect [48], as shown in Fig. S5. The binding energy of He$_n$ clusters to the NGI is positive and linearly increases with a slope of 1.74 eV/atom, suggesting that the energy required for the NGI to trap each atom of He$_n$ is insensitive to the cluster size. The linear behavior of the binding energy may be attributed to the wide two-dimensional channel within the NGI, which can provide excess volume for He$_n$ cluster formation. The binding energy of an additional He to He$_{n-1}$ also presents a positive value whether in the bulk or within the NGI. The local maximum binding energy even reaches 1.66 eV within the NGI (1.05 eV in the bulk), except for the He$_{10}$ cluster. Such high binding energy indicates a strong attractive interaction between He atoms, which motivates He atoms to form He clusters (or small clusters to grow into large clusters) by a self-trapping mechanism. Once a He cluster is formed, dissociating He atoms from the cluster becomes difficult. Different from the linear tendency of the binding energy of He$_n$ to the NGI, the binding energy of an additional He to He$_{n-1}$ exhibits a fluctuant increase with the increasing n, especially the tendency in the bulk, which is consistent with the results of the previous studies [25,46]. This finding may be mainly due to the fact that larger He clusters have stronger attraction on He atoms, and the different displacement fields induced by each additional He lead to the fluctuations in the increment of binding energy. However, the dramatic increase in the binding energy of an additional He to He$_9$ in the bulk may be attributed to the excess He atom inducing the lattice distortion and even SIA emission around the finite interstitial space, as previously mentioned.

In Fig. 5, by comparing the binding energies of an additional He to He$_{n-1}$ in the bulk and within the NGI, the binding energies are found to be higher within the NGI than those in the bulk (apart from n = 10), implying that the trapping strength of He$_{n-1}$ to a He atom within the NGI is stronger, and the He$_n$ is much more stable within the NGI than that in the bulk. In addition, the binding energy of a He atom to He$_{n-1}$ within the NGI shows the largest, followed by that of a He atom to the NGI, and the smallest binding energy of a He atom to He$_{n-1}$ in the bulk. Consequently, He atoms in the vicinity of the NGI prefer to be trapped by the NGI than by the He clusters in the bulk due to the two stronger attractions within the NGI, as exhibited in Figs. 2 and 3. Combined with the dissociation event of He$_4$ observed in Fig. 2(b), it is speculated that all the He atoms in a cluster in the vicinity of the NGI are simultaneously attracted from the cluster itself, other clusters, and the NGI, which depends on the strength of the interactions.

3.3. Formation and binding energies of He$_n$V

The agglomeration of He atoms exacerbates their local stress and can cause the SIA emission, resulting in the formation of vacancies around the cluster. Consequently, He$_n$V$_m$ clusters tend to form in many sites, as shown in Fig. 2. However, relative to the He clusters without vacancies, He$_n$V$_m$ clusters show higher stability near the NGI. The formation and binding energies of He$_n$V (n = 1–10) clusters as a function of the distance from the NGI are shown in Fig. 6 to reveal the effects of the NGI on the formation and growth of He clusters with a Ni monovacancy. Similarly, the endothermic process also appears as a He$_n$V migrates from the bulk to the NGI, and this effect is enhanced with the increasing n, that is, increasing interaction length scale and higher binding energy. These results suggest that He$_n$V clusters also tend to segregate into the NGI. However, compared with He$_n$ clusters, the interaction length scale and the segregation strength of the NGI on He$_n$V clusters are often reduced with the same n, *e.g.*, the decline of 7.2 Å and 3.11 eV of a He$_{10}$ cluster with a monovacancy, suggesting that the pre-existing vacancies may weaken the role of the NGI in trapping He atoms. In addition, the formation and binding energies of He$_n$V clusters

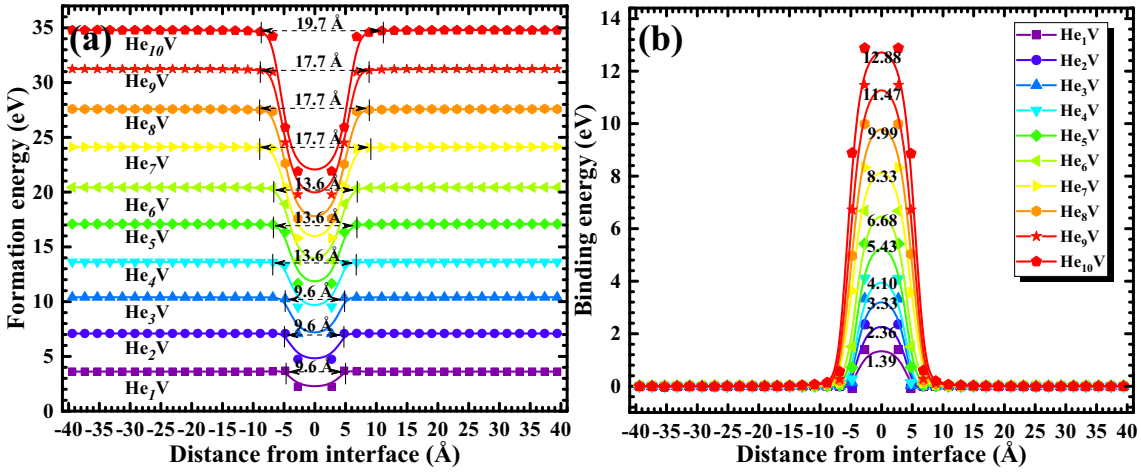

Fig. 6. Formation (a) and binding (b) energies of He$_n$V clusters (n = 1–10) as a function of the distance from the NGI. The interaction length scale and binding energy of the NGI on He$_n$V are marked.

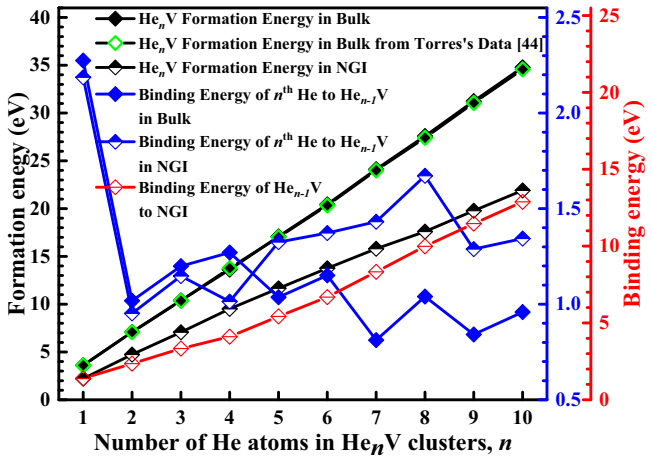

Fig. 7. Energetics of He$_n$V as a function of the number of He atoms, including the formation energies of He$_n$V and the binding energies of an additional He to He$_{n-1}$V in the bulk and within the NGI, as well as the binding energy of He$_n$V to the NGI.

show good consistency without fluctuation in contrast to He$_n$ clusters, implying that the pre-existing vacancies may make the cluster configurations more stable and reduce lattice-atomic displacements.

Similar to He$_n$ clusters, further energetic information of He$_n$V clusters is also analyzed and exhibited in Fig. 7. The formation energy of He$_n$V as a function of He atom number shows a linear increase whether in the bulk or within the NGI. Especially, the results of the bulk are consistent with those of Torres et al. [45]. The energy increases from 3.61 to 34.78 eV in the bulk or from 2.22 to 21.90 eV within the NGI (see Table S1), and the slope of the dependency is determined to be 3.45 or 2.05 eV/atom, respectively, all showing smaller values than those of He$_n$ clusters. The binding energy of He$_n$V to the NGI is positive and linearly increases with the increasing number of He atoms (with a slope of 1.30 eV/atom). The binding energy of an additional He to He$_{n-1}$V also presents positive values whether in the bulk or within the NGI. In the bulk, the binding energy of an additional He to He$_{n-1}$ has a similar trend to that of W [25] and Fe [46]. The binding energy gradually increases for $n = 2$ to 4, which may be due to the fact that the cluster configuration tends to be more stable, as shown in Fig. S1(a–c). Particularly, a local maximum appears when the He$_n$V cluster has four or six He atoms. In these cases, the He atoms easily form a compact tetrahedron (Fig. S1(c)) or octahedron (Fig. S1(e)) with a monovacancy, thus releasing more energy from the system. However, a sudden decrease in the binding energy with the insertion of the seventh He atom indicates the emergence of asymmetry in the configuration and the aggravation of local lattice distortion around the cluster [36,46]. Within the NGI, the binding energy of an additional He to He$_{n-1}$V ($n > 1$) still shows an increasing trend. The binding energy of a He atom to a monovacancy, with 2.19 eV within the NGI or 2.27 eV in the bulk, is distinctly higher than that of a He atom to a He$_{n-1}$V ($n > 1$). In addition, the binding energy of a He atom to the NGI is also lower than that of a He atom to a monovacancy. These results suggest that a monovacancy with low electron density exhibits the strongest ability to capture a single He atom near the NGI and forms the nucleation site for a cluster. Different from the interaction between a He and a He$_{n-1}$, the binding energy of an additional He to He$_{n-1}$V within the NGI is lower than that of the bulk when $n < 5$ but higher when $n \geq 5$. The change can be speculated as follows. When $n < 5$, the vacancy in the He$_{n-1}$V cluster has a stronger attraction on an additional He atom than that of the He atoms in the cluster, and this attraction is more pronounced in the bulk than within the NGI. When $n \geq 5$, the He atoms in the cluster play a dominant role in trapping an additional He atom as compared with the vacancy, and the He cluster configuration within the NGI, generally forming a two-dimensional configuration similar to that of a He$_n$ within the NGI (see Fig. S5), is more beneficial to promote the cluster trapping He atoms than that in the bulk.

Overall, the binding strength between a He$_n$V and the NGI is weaker than that between a He$_n$ and the NGI with the same n (see Table S1). This phenomenon may be due to the existence of recombination/annihilation between the vacancy and He atoms, resulting in the pinning of He atoms by the vacancy and decreasing the segregation strength of the NGI on He$_n$V. By comparing the binding energies of an additional He to He$_{n-1}$ and He$_{n-1}$V ($n > 1$) within the NGI, the vacancy is found to have no remarkable effect on the binding energy possibly due to the tendency of the He atoms in He$_n$V to aggregate into a planar configuration (see Fig. S5), which is similar to that of He$_n$ within the NGI. However, comparing the binding energies of an additional He to a He$_{n-1}$ and a He$_{n-1}$V with the same n in the bulk, a He$_{n-1}$V has stronger attraction on an additional He than that of a He$_{n-1}$ when $n < 8$ because the vacancy can strongly trap He atoms. By contrast, the two kinds of interactions tend to be equal, and even the latter is stronger than the former when $n \geq 8$. The change occurs due to increased local lattice distortion around the He$_{n-1}$ cluster ($n \geq 8$) as previously mentioned, providing excess volume to trap He atoms and resulting in more energy released from the system. Generally, when a defect **A** (*e.g.*, a He atom or vacancy) is introduced in a particular site of crystal, the total volume of the crystal may change because of the displacement field around the defect **A**, which inevitably induces a local stress, tending to expand, contract, or distort the lattice [49–53]. If another defect **B** (*e.g.*, a cluster, GB, or heterointerface) is also present in the crystal, then an interaction will exist between the defects **A** and **B** [49]. According to elasticity theory, the first-order size effect, which is deduced by a continuum elastic model, has the most important contribution to the interaction [54] and only involves the relaxation volume (*i.e.*, lattice expansion or contraction associated with the introduction of defect **A**) and the hydrostatic field of the defect **B** [49,54]. Several studies have also shown that the hydrostatic field of the defect **B** depends on the formation volume of defect **A** [55,56]. Consequently, the binding energy of defect **A** to **B** can be roughly determined by the relaxation and the formation volumes of defect **A**. For example, by using the Voronoi tessellation method implemented in LAMMPS code [37], the formation volumes per He atom in He-related clusters are calculated, as shown in Fig. S6. The formation volume per He atom has a higher value within the NGI than that in the bulk for the same n. The formation volume has a maximum value when a vacancy site has only one He atom. In the bulk, the formation volume per He atom of He$_n$V is initially larger than that of He$_n$ but is roughly equal to that of He$_n$ with the increase in n. Within the NGI, apart from $n = 1$, the formation volume per He atom of He$_n$V is roughly equal to that of He$_n$. The trends of formation volumes show a good consistency with those of the binding energies described above, which demonstrates that the larger the He formation volume is, the higher the binding energy [28,56].

3.4. He diffusion toward/along the NGI

At elevated temperature, the isolated He atoms in the bulk are rarely localized by the surrounding lattice environment but are easy to diffuse randomly. However, due to the presence of the NGI, the isolated He atoms are prone to migration toward the NGI. The different migration paths dependent on the initial positions of He atoms are observed herein to reveal possible migration mechanisms. Different from the shifting and rotation mechanisms of SIAs [7], the He atoms can migrate along the pathway connecting two TIS nearest to each other in the Ni[111] direction [33]. Wherein the intermediate path image is located at the OIS in the middle of the two TIS. By using the CI-NEB method, the kinetic process for a He atom to migrate along a TIS–OIS–TIS pathway is calculated, as shown in Fig. 8(a). The He diffusion barrier in the bulk is 0.124 ± 0.002 eV in agreement with the previous result of pure Ni [33]. However, the He diffusion barrier

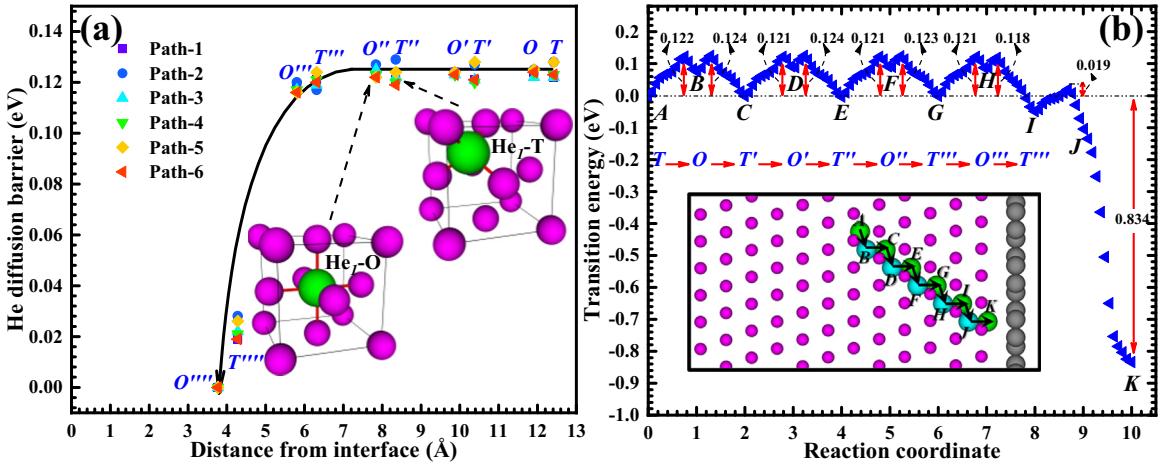

Fig. 8. He diffusion toward the NGI. (a) He diffusion barriers as a function of the distance from the NGI along six different paths. The black arrows are drawn only as a guide to the eyes. A tetrahedral interstitial He and an octahedral interstitial He corresponding to two different final states are exhibited in the insets. (b) A path for He diffusion from the bulk to the NGI. The system energy at position A is selected as the reference energy. After the He migrates from position A to K, the system energy decreases by 0.834 eV. The inset corresponds to the He in different positions along the diffusion path.

reduces to zero when the He enters into the NGI because He atoms within a certain range of the NGI are spontaneously trapped by the NGI, indicating that He atoms really prefer to migrate toward the NGI. In addition, one typical diffusion path of a He atom is also shown in Fig. 8(b), which demonstrates that a tetrahedral interstitial He atom needs to temporarily move to its adjacent OIS before jumping to the next TIS. The He atom must overcome a low barrier of 0.019 eV to move toward the NGI; meanwhile, the system energy reduces by 0.834 eV when the He is located at the NGI. Overall, the kinetic results indicate that the He atoms in the vicinity of NGI preferentially migrate toward the NGI with an extremely low diffusion energy barrier as an alternative driving force apart from the aforementioned energetics. Consequently, the He concentration tends to reduce, and the clustering and growth rates of He atoms are slowed down in the bulk.

As shown in Fig. 3, the He atoms within the NGI are more easily to migrate, and even large He clusters can also move fast. To clarify this issue, the different stable sites of He atoms within the NGI are first searched by multiple configuration optimization approach, that is, placing the He atoms at the potentially relevant interstitial sites and subsequently relaxing the system, and the results are respectively shown in Fig. 9(a) and (b). Clearly, He atoms have only two types of stable sites and are periodically arranged into hexagons within the NGI; both sites are colored as green (G) and red (R) spheres. Further observations revealed that both types of He atoms prefer to be located at the center of a tetrahedron comprising three Ni atoms and one C atom (Fig. 9(c) and (d)), which may be beneficial to stabilize their configurations. The difference of He atoms in the stable sites may be due to the slight lattice mismatch between Gr and Ni(111) in-plane lattice constants [7], which induces a difference in the local lattice environment around the He atoms. The formation energies of He atoms at different stable sites are shown in Fig. 9(e). The formation energies at the G and R sites are approximately 3.450 and 3.506 eV, respectively, implying that the G sites are stable for He atoms within the NGI. After extensive tests evaluated by the CI-NEB method, direct jumps between two adjacent G (or R) sites are found to be impossible because the energy landscape exhibits a local maximum along this path without a saddle point. Hence, only migrations along a G–R–G pathway are feasible. One typical diffusion path of He atoms along the NGI is shown in Fig. 9(f) (details in Supplementary Movie 4). It can be seen that a He atom within the NGI prefers to jump along a zigzag path and must overcome an energy barrier of approximately 0.08 eV from G to R site or approximately 0.06 eV from R to G site. However, the final energy of the system is unaffected after the diffusion is completed. The same phenomena are also observed in other diffusion paths exhibited in Fig. S7. The diffusion barriers are considerably lower than those in the bulk, further proving that He atoms are easier to migrate within the NGI than in the bulk. Consequently, He atoms are more likely to form large clusters within the NGI because of the low diffusion barrier and high binding energy.

4. Conclusions

In summary, the effects of NGIs on the nucleation and growth of He-related clusters are explored from the perspectives of thermodynamics, energetics, and kinetics by using atomistic simulations. The MD simulations show that isolated He atoms prefer to attract each other in the bulk. The accompanying He clusters would constantly trap He atoms and even emit SIAs to form more stable He_nV_m clusters. It is of interest to note that the nucleation and growth rates of He-related clusters in the bulk would be slowed down by the NGI. The NGI can trap isolated He atoms and small He clusters from the bulk, resulting in a remarkable reduction in He atoms in the bulk. Relative to the He clusters without vacancies, He_nV_m clusters are more difficult to be trapped by the NGI due to their low mobilities. The He atoms/clusters within the NGI can easily migrate on the surfaces of the NGI, thus leading to the formation of larger He-related clusters than those in the bulk. The MS and CI-NEB calculations of small clusters have been employed to understand the aforementioned phenomena. Both He_n and He_nV (n = 1–10) clusters tend to segregate into the NGI because they have lower formation energies within the NGI than those in the bulk. The segregation strength increases with the increase in n due to the large interaction length and high binding energy. The binding energy of an additional He to He_{n-1}/$He_{n-1}V$ presents a positive value whether in the bulk or within the NGI, indicating that He clusters grow by self-trapping. The trapping strength of He_{n-1}/$He_{n-1}V$ to a He atom within the NGI is often stronger, and the He_n/He_nV is much more stable within the NGI than that in the bulk. $He_{n-1}V$ usually exhibits stronger attraction on an additional He than that of He_{n-1}. Vacancies can be cluster nucleation sites because of their strong interactions with He atoms, thus resulting in weakened ability of the NGI to trap He atoms/clusters. The energy barrier for He atoms to diffuse into the NGI reduces to zero, and the diffusion barriers of He atoms within the NGI are lower than those in the bulk. The current investigation significantly enhances our understanding of the He damage behaviors in NGNLs. It is likely to design the NGIs to form a network, thus providing continuous pathways to achieve the fast and unimpeded diffusion of He atoms/clusters and promote He releasing

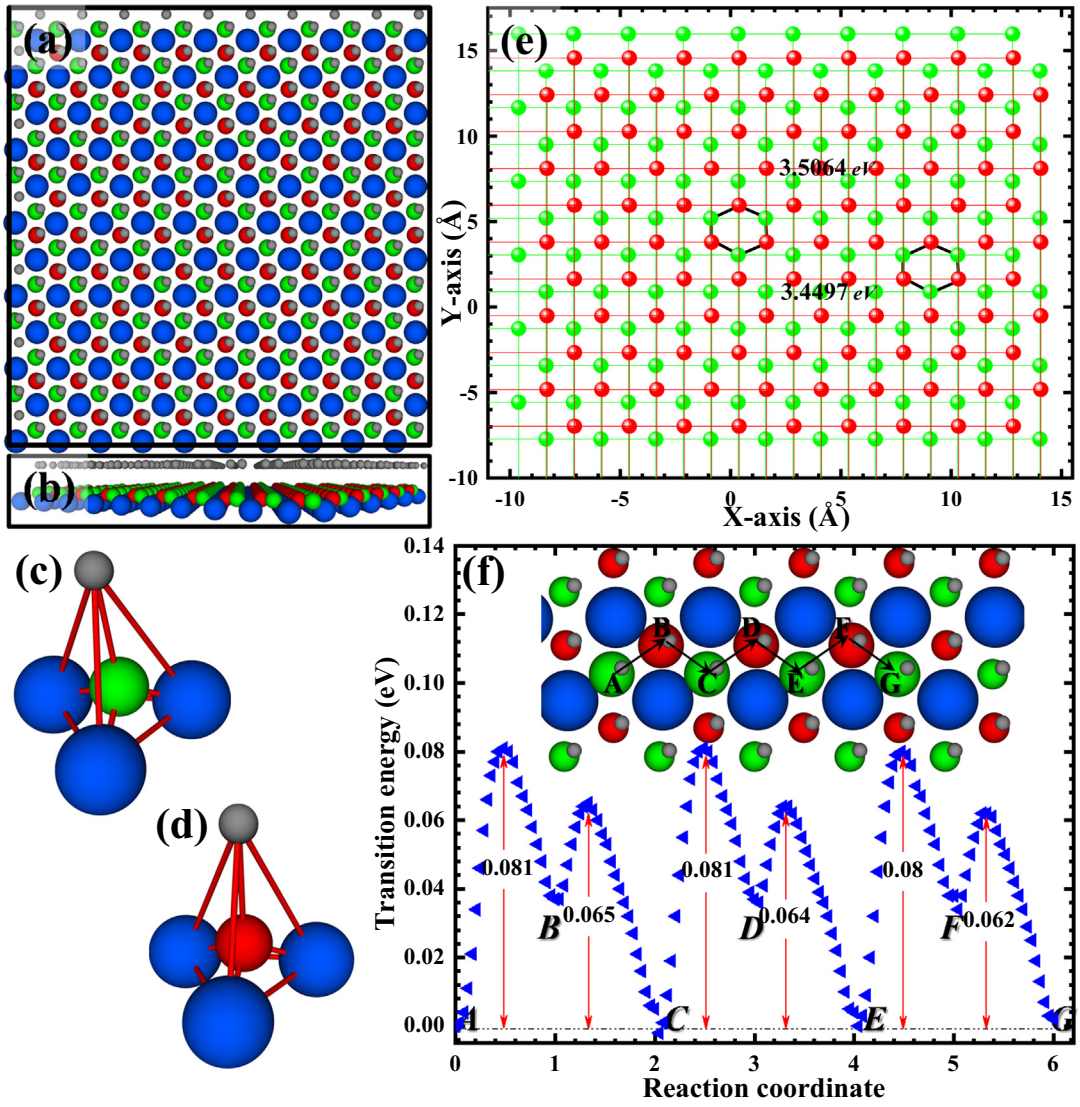

Fig. 9. He diffusion along the NGI. (a) Different stable sites of He atoms within the NGI observed from the top view, where only two types of stable sites for He exist within the NGI and are colored as green (G) and red (R) spheres. (b) Different stable sites of He atoms within the NGI observed from a side view, (c) stable configuration of He atom at a G site, and (d) stable configuration of He atom at an R site. (e) Formation energies of He atoms at different stable sites within the NGI, with the values of 3.450 eV at a G site or 3.506 eV at an R site. (f) A path for He diffusion along the NGI. The system energy at position A is selected as the reference energy. After the He migrates from position A to G, the system energy remains the same.

from the system. Consequently, He-assisted mechanical degradation due to He accumulation in materials may be further delayed.

Supplementary data to this article can be found online at https://doi.org/10.1016/j.apsusc.2019.05.085.

Acknowledgement

H. Huang thanks Yuanyuan Yu for positive encouragement and the passionate help of Tao Lu and Chenguang Liu in the work. This work was supported by the National Natural Science Foundation of China (Grant No. 11705087), the Natural Science Foundation of Jiangsu Province (Grant No. BK20170776), the Fundamental Research Funds for the Central Universities (Grant No. NJ20150021 & NT2018018), and the Open Fund of Key Laboratory of Materials Preparation and Protection for Harsh Environment (Nanjing University of Aeronautics and Astronautics), Ministry of Industry and Information Technology of the People's Republic of China (Grant No. 56XCA18159-2).

References

[1] S. Si, W. Li, X. Zhao, M. Han, Y. Yue, W. Wu, S. Guo, X. Zhang, Z. Dai, X. Wang, X. Xiao, C. Jiang, Significant radiation tolerance and moderate reduction in thermal transport of a tungsten nanofilm by inserting monolayer graphene, Adv. Mater. 29 (2017) 1604623.
[2] Y. Kim, J. Baek, S. Kim, S. Kim, S. Ryu, S. Jeon, S.M. Han, Radiation resistant vanadium-graphene nanolayered composite, Sci. Rep. 6 (2016) 24785.
[3] H. Huang, X. Tang, F. Chen, J. Liu, X. Sun, L. Ji, Radiation tolerance of nickel–graphene nanocomposite with disordered graphene, J. Nucl. Mater. 510 (2018) 1–9.
[4] K.P. So, D. Chen, A. Kushima, M. Li, S. Kim, Y. Yang, Z. Wang, J.G. Park, Y.H. Lee, R.I. Gonzalez, M. Kiwi, E.M. Bringa, L. Shao, J. Li, Dispersion of carbon nanotubes in aluminum improves radiation resistance, Nano Energy 22 (2016) 319–327.
[5] S. Sadeghzadeh, On the oblique collision of gaseous molecules with graphene nanosheets, Mol. Simulat. 42 (2016) 1233–1241.
[6] T. Yang, L. Yang, H. Liu, H. Zhou, S. Peng, X. Zhou, F. Gao, X. Zu, Ab initio study of stability and migration of point defects in copper-graphene layered composite, J. Alloy Compd. 692 (2017) 49–58.
[7] H. Huang, X. Tang, F. Chen, F. Gao, Q. Peng, L. Ji, X. Sun, Self-healing mechanism of irradiation defects in nickel-graphene nanocomposite: an energetic and kinetic perspective, J. Alloy. Comp. 765 (2018) 253–263.
[8] I.J. Beyerlein, A. Caro, M.J. Demkowicz, N.A. Mara, A. Misra, B.P. Uberuaga, Radiation damage tolerant nanomaterials, Mater. Today 16 (2013) 443–449.
[9] X. Zhang, K. Hattar, Y. Chen, L. Shao, J. Li, C. Sun, K. Yu, N. Li, M.L. Taheri,

H. Wang, J. Wang, M. Nastasi, Radiation damage in nanostructured materials, Prog. Mater. Sci. 96 (2018) 217–321.
[10] X. Sun, F. Chen, H. Huang, J. Lin, X. Tang, Effects of interfaces on the helium bubble formation and radiation hardening of an austenitic stainless steel achieved by additive manufacturing, Appl. Surf. Sci. 467 (2019) 1134–1139.
[11] X.M. Bai, A.F. Voter, R.G. Hoagland, M. Nastasi, B.P. Uberuaga, Efficient annealing of radiation damage near grain boundaries via interstitial emission, Science 327 (2010) 1631–1634.
[12] F. Chen, X. Tang, H. Huang, J. Liu, H. Li, Y. Qiu, D. Chen, Surface damage and mechanical properties degradation of Cr/W multilayer films irradiated by Xe20+, Appl. Surf. Sci. 357 (2015) 1225–1230.
[13] A.F. Rowcliffe, L.K. Mansur, D.T. Hoelzer, R.K. Nanstad, Perspectives on radiation effects in nickel-base alloys for applications in advanced reactors, J. Nucl. Mater. 392 (2009) 341–352.
[14] M.A. Stopher, The effects of neutron radiation on nickel-based alloys, Mater. Sci. Tech. 33 (2017) 518–536.
[15] J. Gao, L. Bao, H. Huang, Y. Li, Q. Lei, Q. Deng, Z. Liu, G. Yang, L. Shi, ERDA, RBS, TEM and SEM characterization of microstructural evolution in helium-implanted Hastelloy N alloy, Nucl. Instrum. Meth. B 399 (2017) 62–68.
[16] T.M. Angeliu, J.T. Ward, J.K. Witter, Assessing the effects of radiation damage on Ni-base alloys for the prometheus space reactor system, J. Nucl. Mater. 366 (2007) 223–237.
[17] C. Wang, C. Ren, W. Zhang, H. Gong, P. Huai, Z. Zhu, H. Deng, W. Hu, A molecular dynamics study of helium diffusion and clustering in fcc nickel, Comput. Mater. Sci. 107 (2015) 54–57.
[18] L. Luneville, J.C. Sublet, D. Simeone, Impact of nuclear transmutations on the primary damage production: the example of Ni based steels, J. Nucl. Mater. 505 (2018) 262–266.
[19] N. Li, M. Demkowicz, N. Mara, Y. Wang, A. Misra, Hardening due to interfacial He bubbles in nanolayered composites, Mater. Res. Lett. 4 (2016) 75–82.
[20] C. Lu, Z. Lu, R. Xie, C. Liu, L. Wang, Microstructure of HIPed and SPSed 9Cr-ODS steel and its effect on helium bubble formation, J. Nucl. Mater. 474 (2016) 65–75.
[21] X. Wang, L. Niu, S. Wang, Strong trapping and slow diffusion of helium in a tungsten grain boundary, J. Nucl. Mater. 487 (2017) 158–166.
[22] W. Guo, L. Cheng, G. De Temmerman, Y. Yuan, G. Lu, Retarded recrystallization of helium-exposed tungsten, Nucl. Fusion 58 (2018) 106011.
[23] L. Yang, F. Gao, R.J. Kurtz, X. Zu, Atomistic simulations of helium clustering and grain boundary reconstruction in alpha-iron, Acta Mater. 82 (2015) 275–286.
[24] P. Yvon, M. Le Flem, C. Cabet, L.J. Seran, Structural materials for next generation nuclear systems: challenges and the path forward, Nucl. Eng. Des. 294 (2015) 161–169.
[25] X. Li, Y. Liu, Y. Yu, G. Luo, X. Shu, G. Lu, Helium defects interactions and mechanism of helium bubble growth in tungsten: a molecular dynamics simulation, J. Nucl. Mater. 451 (2014) 356–360.
[26] J. Xu, C. Wang, W. Zhang, C. Ren, H. Gong, P. Huai, Atomistic simulations of the interactions of helium with dislocations in nickel, Nucl. Mater. Energ. 7 (2016) 12–19.
[27] Y.N. Osetsky, R.E. Stoller, Atomic-scale mechanisms of helium bubble hardening in iron, J. Nucl. Mater. 465 (2015) 448–454.
[28] M.A. Tschopp, F. Gao, K.N. Solanki, Binding of He_nV clusters to α-Fe grain boundaries, J. Appl. Phys. 115 (2014) 233501.
[29] H. Deng, W. Hu, F. Gao, H.L. Heinisch, S.Y. Hu, Y. Li, R.J. Kurtz, Diffusion of small He clusters in bulk and grain boundaries in α-Fe, J. Nucl. Mater. 442 (2013) S667–S673.
[30] J. Marian, C.S. Becquart, C. Domain, S.L. Dudarev, M.R. Gilbert, R.J. Kurtz, D.R. Mason, K. Nordlund, A.E. Sand, L.L. Snead, T. Suzudo, B.D. Wirth, Recent advances in modeling and simulation of the exposure and response of tungsten to fusion energy conditions, Nucl Fusion 57 (2017) 092008.
[31] M.G. McPhie, L. Capolungo, A.Y. Dunn, M. Cherkaoui, Interfacial trapping mechanism of He in Cu–Nb multilayer materials, J. Nucl. Mater. 437 (2013) 222–228.
[32] E. Torres, J. Pencer, Molecular dynamics study of the role of symmetric tilt grain boundaries on the helium distribution in nickel, J. Nucl. Mater. 502 (2018) 86–94.
[33] E. Torres, J. Pencer, D.D. Radford, Density functional theory-based derivation of an interatomic pair potential for helium impurities in nickel, J. Nucl. Mater. 479 (2016) 240–248.
[34] L. Hu, K.D. Hammond, B.D. Wirth, D. Maroudas, Interactions of mobile helium clusters with surfaces and grain boundaries of plasma-exposed tungsten, J. Appl. Phys. 115 (2014) 173512.
[35] M.A. Tschopp, F. Gao, K.N. Solanki, He–V cluster nucleation and growth in α-Fe grain boundaries, Acta Mater. 124 (2017) 544–555.
[36] H. Gong, C. Wang, W. Zhang, P. Huai, W. Lu, Z. Zhu, Atomistic simulation of the trapping capability of He-vacancy defects at Ni grain boundary, Model. Simu. Mater. SC 24 (2016) 085004.
[37] S. Plimpton, Fast parallel algorithms for short-range molecular dynamics, J. Comput. Phys. 117 (1995) 1–19.
[38] A. Stukowski, Visualization and analysis of atomistic simulation data with OVITO–the Open Visualization Tool, Model. Simul. Mater. Sci. 18 (2009) 015012.
[39] G. Bonny, N. Castin, D. Terentyev, Interatomic potential for studying ageing under irradiation in stainless steels: the FeNiCr model alloy, Model. Simul. Mater. Sci. 21 (2013) 085004.
[40] S.J. Stuart, A.B. Tutein, J.A. Harrison, A reactive potential for hydrocarbons with intermolecular interactions, J. Chem. Phys. 112 (2000) 6472–6486.
[41] D.E. Beck, A new interatomic potential function for helium, Mol. Phys. 14 (1968) 311–315.
[42] S.P. Huang, D.S. Mainardi, P.B. Balbuena, Structure and dynamics of graphite-supported bimetallic nanoclusters, Surf. Sci. 545 (2003) 163–179.
[43] R.E. Tuzun, D.W. Noid, B.G. Sumpter, R.C. Merkle, Dynamics of flow inside carbon nanotubes, Nanotechnology 8 (1997) 112.
[44] E. Jin, S. Du, M. Li, C. Liu, S. He, J. He, H. He, Influence of helium atoms on the shear behavior of the fiber/matrix interphase of SiC/SiC composite, J. Nucl. Mater. 479 (2016) 504–514.
[45] E. Torres, C. Judge, H. Rajakumar, A. Korinek, J. Pencer, G. Bickel, Atomistic simulations and experimental measurements of helium nano-bubbles in nickel, J. Nucl. Mater. 495 (2017) 475–483.
[46] F. Gao, H. Deng, H.L. Heinisch, R.J. Kurtz, A new Fe–He interatomic potential based on ab initio calculations in α-Fe, J. Nucl. Mater. 418 (2011) 115–120.
[47] H. Gong, C. Wang, W. Zhang, J. Xu, P. Huai, H. Deng, W. Hu, The energy and stability of helium-related cluster in nickel: a study of molecular dynamics simulation, Nucl. Instrum. Meth. B 368 (2016) 75–80.
[48] N. Gao, M. Victoria, J. Chen, H. Van Swygenhoven, Helium-vacancy cluster in a single bcc iron crystal lattice, J. Phys-Condens. Mat. 23 (2011) 245403.
[49] K.M. Miller, A study of point and planar defects in copper, Phys. Status Solidi B 98 (1980) 387–399.
[50] H. Zhou, S. Jin, Y. Zhang, G. Lu, Anisotropic strain enhanced hydrogen solubility in bcc metals: the independence on the sign of strain, Phys. Rev. Lett. 109 (2012) 135502.
[51] K.E. Eshkalak, S. Sadeghzadeh, M. Jalaly, Studying the effects of longitudinal and transverse defects on the failure of hybrid graphene-boron nitride sheets: a molecular dynamics simulation, Phys. E. 104 (2018) 71–81.
[52] K.E. Eshkalak, S. Sadeghzadeh, M. Jalaly, Mechanical properties of defective hybrid graphene-boron nitride nanosheets: a molecular dynamics study, Comput. Mater. Sci. 149 (2018) 170–181.
[53] S. Sadeghzadeh, Computational design of graphene sheets for withstanding the impact of ultrafast projectiles, J. Mol. Graph. Model. 70 (2016) 196–211.
[54] R. Bullough, R.C. Newman, The kinetics of migration of point defects to dislocations, Rep. Prog. Phys. 33 (1970) 101.
[55] X. Zhou, D. Marchand, D.L. McDowell, T. Zhu, J. Song, Chemomechanical origin of hydrogen trapping at grain boundaries in fcc metals, Phys. Rev. Lett. 116 (2016) 075502.
[56] A. Hallil, A. Metsue, A. Oudriss, J. Bouhattate, X. Feaugas, Segregation energy of the hydrogen at Ni grain boundaries: some implications of the atomic volume and the interstitial self-stress, J. Mater. Sci. 53 (2018) 5356–5363.